Aligning Quadripolar Electrodes within Ultrasound Waveform Maximizes Acoustoelectric Signal

Alec Bales-D'Cruze[1], Sathiyamoorthy Selladurai[1], Andy Adler[1], Nicola Schieda[2], and Carlos Rossa[1]
[1]*Department of Systems and Computer Engineering, Carleton University, Ottawa, Canada.*
[2]*Dep. of Radiology, Radiation Oncology and Medical Physics, University of Ottawa, Ottawa, ON, Canada*
alecbalesdcruze@cmail.carleton.ca; selladuraisathiyamoo@cunet.carleton.ca;
adler@sce.carleton.ca; nschieda@toh.ca; carlos.rossa@carleton.ca

***Abstract*—Acoustoelectric tomography (AET) maps the electrical conductivity of a medium by locally modulating it with ultrasound. These localized perturbations in conductivity alter an externally applied electrical field driven through the tissue by stimulating electrodes. The acoustoelectric (AE) effect is extremely small and difficult to measure reliably, especially in minimal AET, where only a limited number of electrodes are placed inside the medium to acquire images directly from within. In minimal AET, the position of these electrodes relative to regions excited by ultrasonic pressure strongly influences the generated signal.**

This paper investigates optimal electrode placement using a quadripolar configuration consisting of two stimulating electrodes and two measuring electrodes. We implement a finite element model of the acoustoelectric effect and compare the measured signals in the presence and absence of medium inclusions. The results show that the signal is maximized when the quadripolar electrodes are aligned with the direction of ultrasound wave propagation, providing insights to guide the development of surgical tools equipped with internal electrodes for minimal AET imaging.

I. Introduction

Acoustoelectric tomography (AET) is an emerging medical imaging modality that combines the contrast of electrical impedance tomography with the spatial resolution of ultrasound, enabling high-contrast, high-resolution imaging of tissue conductivity [1]. AET is fundamentally based on the acoustoelectric (AE) effect, a physical coupling that links localized acoustic pressure to small changes in tissue conductivity [2], [3], [4]. As a pressure wave propagates through the tissue, it induces cycles of compression and rarefaction in tissue cells, altering the tissue's local electrical conductivity proportional to the magnitude of the applied pressure. When the tissue is subjected to an external electrical current, these spatially encoded conductivity modulations alter the electric field within the tissue and can be detected as voltage modulations induced at the same frequency of the applied ultrasonic wave using surface or implanted electrodes. By steering the acoustic pressure field, sufficient information can be acquired to reconstruct a detailed map of the tissue's electrical conductivity [1], [5], [6].

Traditionally, AET relies on several electrodes placed on the tissue surface, where electrode placement strongly influences the richness and information captured in the measured signal. Surface electrodes can maximize signal strength and sensitivity to heterogeneous target regions near the tissue surface; however, the sensitivity of these measurements decreases rapidly with depth [2]. Internal electrodes embedded in surgical tools, such as needles or catheters, may provide an alternative to maintain sensitivity to target regions deeper in the tissue. Still, with a limited number of internal electrodes, their placement with respect to the ultrasound wave and target region has an even stronger influence on the measured signal [7], [8], [9].

A basic AET setup uses a pair of electrodes to stimulate the tissue with a direct or alternating electric current of fixed magnitude, and one or more pairs to measure the induced voltage. Several techniques have been proposed to demodulate the high-frequency component of the measured signal (which matches the ultrasound waveform centre frequency) from the low-frequency carrier signal (which matches the stimulating current frequency). For example, lock-in amplifiers [10], low-noise differential amplifiers with passive bandpass filters [11], and high-pass filters into differential amplifiers with digital filtering [12] have been used to detect and filter the signal.

The AE effect is extremely small due to a weak coupling constant and the surrounding environment noise. Previous studies have found that placing the exciting and measuring electrodes in line with the direction of ultrasound beam propagation can maximize the AE signal strength [2], [13]. An important consideration that has not been systematically studied is not only how such electrode placement affects signal strength, but more fundamentally how it alters the system's spatial sensitivity to internal target regions with higher or lower conductivity than their surroundings, a key requirement upon which inverse image reconstruction rests [7], [14], [15], [16].

In this paper, we develop a finite element model of the AE effect to evaluate how internal quadripolar electrode placement within tissue affects the magnitude of the measured AE signal and the sensitivity to target regions of differing conductivity. To this end, we implement a finite-element mesh representing

This research is supported by the Ontario Graduate Scholarship and the Ontario Ministry of Colleges and Universities Early Researcher Award.

We acknowledge the support of the Government of Canada's New Frontiers in Research Fund (NFRF), [NFRFE-2024-00317].

Nous remercions le fonds Nouvelles frontières en recherche du gouvernement du Canada de son soutien [NFRFE-2024-00317].

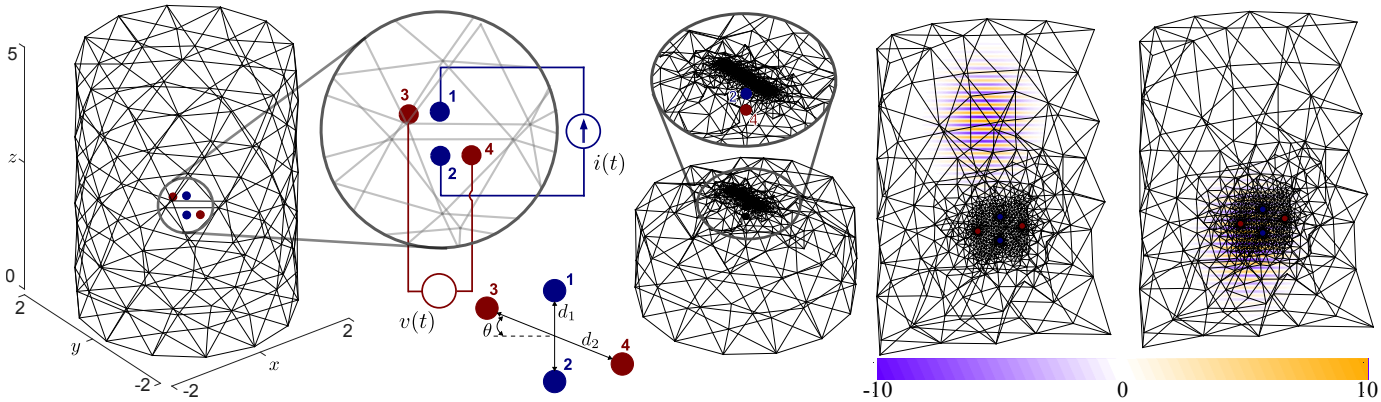

Fig. 1: Simulation model in EIDORS. The tissue is presented as a cylindrical mesh having a radius of 20 mm and a height of 50 mm. The electrodes are spherical with a radius of 0.5 mm. Electrodes 1 and 2 create an electric field and remain stationary, while electrodes 3 and 4 are rotated around the centre of the mesh while measuring the induced voltage. The distance between the electrodes is set to $d_1 = 4$ mm and $d_2 = 8$ mm so that the electrodes do not collide while completing a half rotation from $\theta = 0°$ to $\theta = 180°$ in increments of $4.5°$. As the region of interest is located at the centre of the mesh nearest to the electrodes, a denser mesh is created to improve the accuracy of the simulation results (centre figure). The figure on the right shows the simulated ultrasound waveform passing through the mesh, inducing a change in voltage through the AE effect. A 1 mm radius inclusion with variable conductivity is placed at the centre of the mesh.

tissue with internal quadripolar electrodes using the Electrical Impedance Tomography and Diffuse Optical Tomography Reconstruction Software (EIDORS) [17]. The ultrasound waveform is approximated as a spherical, time-and spatially-dependent Gaussian distribution of altered tissue conductivity that propagates through the mesh at the speed of sound. With the proposed framework, we conduct simulations over 200 distinct electrode and tissue conductivity configurations and evaluate the AE signal strength in the presence and absence of an internal inclusion with lower and higher conductivity. By comparing signal strength in homogeneous and heterogeneous models, we determine not only the electrode configuration that maximizes the measured AE signal but also the influence of the inclusion's conductivity on signal strength. To the best of the authors' knowledge, such a study has not been reported before.

This paper is structured as follows: The finite element model implemented in EIDORS and the ultrasound waveform approximation model are presented in Section II. The different evaluated simulation scenarios are described in Section III, followed by the results. Section IV analyzes the results and their implications for optimizing AET methods with a minimal number of internal electrodes.

II. AE Effect Finite Element Simulation

Similar to electrical impedance tomography, the goal of AET is to map tissue conductivity, but with fewer electrodes and higher spatial resolution. To simulate localized regions of higher or lower conductivity representing an inclusion in the mesh, let $\sigma_0(x, y, z)$ be the background conductivity assigned to every element in the mesh, where x, y, z represent the Cartesian coordinates of any mesh point, and $\Delta\sigma_{ROI}(x, y, z)$ represent regions of altered conductivity. The term $\Delta\sigma_{ROI}(x, y, z)$ is spatially dependent and zero everywhere except for the defined region of interest (ROI). The total mesh conductivity is:

$$\sigma_0(x, y, z) = \sigma_b(x, y, z) + \Delta\sigma_{ROI}(x, y, z). \tag{1}$$

In the simulations, the ROI is centred in the mesh.

A. Modelling the AE Effect

The AE effect describes a change in conductivity when the tissue (or mesh in the proposed model) is subjected to an acoustic pressure. If $\sigma_0(x, y, z)$ is the unperturbed mesh conductivity (in the absence of acoustic pressure), the AE effect changes the local mesh conductivity proportionally to the applied acoustic pressure $\Delta P(x, y, z)$. The change in conductivity $\Delta\sigma(x, y, z)$ takes the form:

$$\frac{\Delta\sigma(x, y, z)}{\sigma_0(x, y, z)} = K\Delta P(x, y, z) \tag{2}$$

where K represents the AE coupling constant in Pa^{-1}, assumed to be the same anywhere in the mesh. In experimental observation, K is in the order of $10^{-9}Pa^{-1}$ in 0.9% saline solution, which is a typical approximation used for the human body [18], [19], [20]. While the coupling constant is assumed to be constant throughout the medium in a realistic scenario it would change proportional to the AE parameters of the medium. The change in pressure $\Delta P(x, y, z)$ is time-dependent, and can be modelled in time and space as:

$$\Delta P(x, y, z, t) = P_0 b(x, y, z, t), \tag{3}$$

where P_0 is the peak amplitude of the acoustic pressure, and $b(x, y, z, t)$ controls the shape of the ultrasound beam at (x, y, z) in the mesh, to be modelled later. The pressure propagates through the mesh over time t. With the above, the

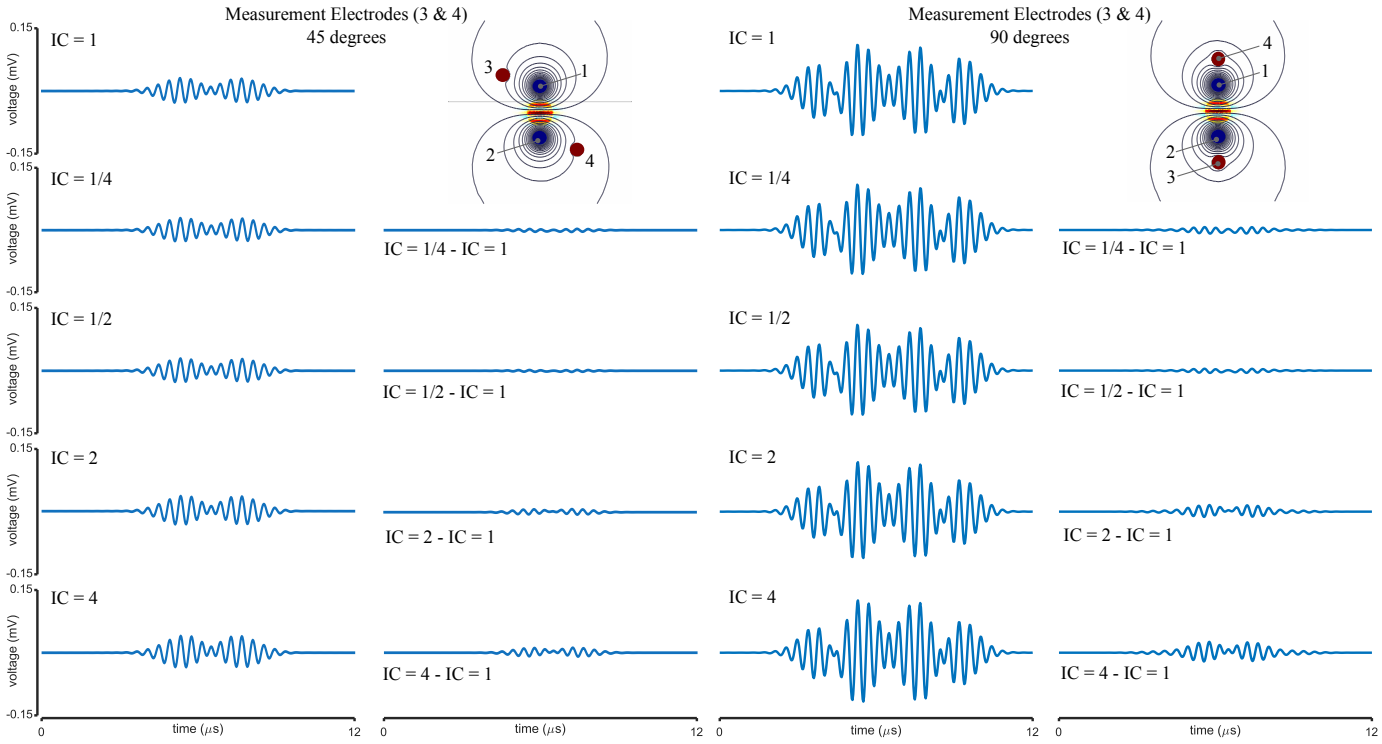

Fig. 2: Voltage measured by electrodes 3 and 4 when at a 45° (first column) and 90° (third column). The first row shows the homogeneous case (with inclusion conductivity $IC = 1$), and the second to fifth rows show the measured waveforms with inclusions of lower ($IC < 1$) and higher ($IC > 1$) conductivities than the background. The second and fourth columns show the voltage difference between the homogeneous and non-homogeneous cases for electrode orientations of 45° and 90°, respectively. The electrical field in EIDORS, along with corresponding electrode positions, is also shown.

AE effect is integrated with the EIDORS mesh by updating the mesh conductivity at (x, y, z, t) as

$$\sigma(x, y, z, t) = \sigma_0(x, y, z) + \Delta\sigma(x, y, z, t). \tag{4}$$

By combining (4) with (2), the updated mesh conductivity that results from the simulated acoustic pressure propagating through the mesh is:

$$\sigma(x, y, z, t) = \sigma_0[1 + K\Delta P(x, y, z, t)]. \tag{5}$$

B. AE Effect as Pulsed Conductivity Changes in 3D

To simulate the propagation of an acoustic pressure through the mesh emulating the AE effect, a wavelet can be used to approximate the pressure field in (3) [10]. Using the real part of a Gabor wavelet, the spatial distribution of the pressure as a function of x, y, z at time t can be modelled as:

$$b(x, y, z) = e^{-\left[\frac{(x-x_c)^2+(y-y_c)^2}{\sigma_{xy}} + \frac{(z-z_c)^2}{\sigma_z}\right]} \cos\left[\omega_0(z - z_c)\right] \tag{6}$$

where x_c, y_c, and z_c are the central points of the Gaussian envelope, and σ_{xy} controls the width of the wavelet, which is symmetrically attenuated along the x and y directions. The width of the Gaussian envelope along z, that is, σ_z, is defined separately to allow the wavelet shape to be independently scaled in the direction of propagation. The cosine term in (6) replicates sinusoidal variations of the ultrasound pulse along the z direction, where ω_0 determines the spatial frequency. As the beam is designed to propagate in the z direction and z_c represents the beam's central point, the latter can be moved in space to represent the wave's propagation in time. By making $z_c = vt$ where v is the speed of sound and t is time, (6) is made dependent on time

$$b(x, y, z, t) = e^{-\left[\frac{(x-x_c)^2+(y-y_c)^2}{\sigma_{xy}} + \frac{(z-vt)^2}{\sigma_z}\right]} \cos\left[\omega_0(z - vt)\right]. \tag{7}$$

The geometry of this waveform was chosen to analytically approximate a focused ultrasound wave close to the central focusing region. With the main purpose of this analytical model to be simpler to implement in the simulator.

C. Simulation Design

Fig. 1 shows the tetrahedral mesh implemented in EIDORS, representing the tissue, with four electrodes placed in a quadripolar configuration at the centre of the mesh. The electrodes are spherical with a radius of 0.5 mm. Electrodes 1 and 2 are fixed in place with a spacing of $d_1 = 4$ mm to deliver a constant electric current of $i(t) = 10$ mA. Electrodes 3 and 4 are also positioned at the centre of the mesh and measure the induced voltage $v(t)$. They are spaced by $d_2 = 2d_1$ mm, and their orientation angle θ relative to the xy plane is swept from 0° to 180° in 41 increments to determine the orientation

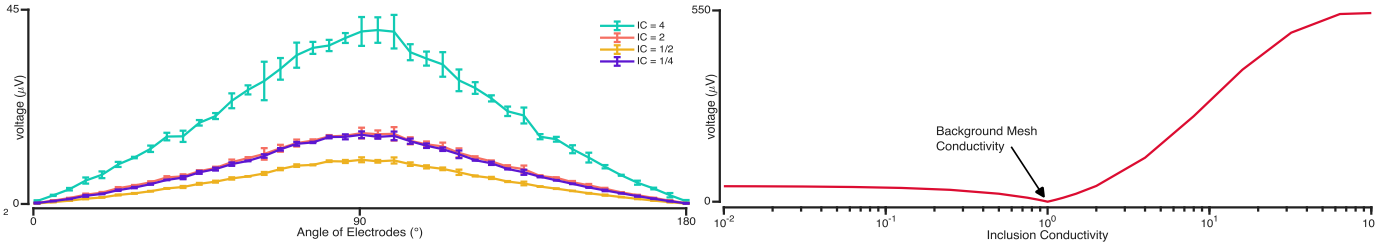

Fig. 3: Peak-to-peak voltage difference between the homogeneous medium and media with an inclusion of higher ($IC > 1$) or lower ($IC < 1$) conductivity as a function of the measuring electrode orientation angle (left), and measured at 90° for inclusion conductivities ranging from 1/1024 to 1024 S/m on a semi-logarithmic scale (right).

that provides the greatest signal strength. This simulation model solves the forward problem in electrical impedance tomography: given the applied electrical current and mesh conductivity, the electrical field can be estimated anywhere in the mesh.

The conductivity of elements in the EIDORS mesh is modulated by (6). The induced voltage resulting from these perturbations is then calculated for each iteration step as the wave passes through the mesh at the speed of sound. The simulation is repeated as the orientation angle of the measuring electrodes is changed. First, a baseline stimulation is run where the conductivity of the mesh is homogeneous everywhere. Then, using the $\Delta\sigma_{ROI}$ in 1, a spherical region of altered but constant conductivity is defined at the centre of the electrodes, referred to as an inclusion. The radius of the inclusion is $r = 1$ mm $< d_1 < d_2$ so that the electrodes are always positioned outside the inclusion. The inclusion conductivity is assigned values both higher and lower than the background and compared with the homogeneous measurements to investigate how the inclusion affects signal strength and characteristics.

III. Simulation Results

In all simulations, the background mesh conductivity is set to $\sigma_b(x, y, z) = 1$ S/m. Five different inclusion conductivities are simulated: A homogeneous mesh ($\Delta\sigma_{ROI}(x, y, z) = 0$), two meshes with a lower inclusion conductivity set to 1/4 and 1/2 of the background conductivity (that is, $\Delta\sigma_{ROI}(x, y, z) = -3/4$ and $\Delta\sigma_{ROI}(x, y, z) = -1/2$, respectively), and two meshes with inclusion conductivity 2 and 4 times higher than the background conductivity (that is, $\Delta\sigma_{ROI}(x, y, z) = 1$ and $\Delta\sigma_{ROI}(x, y, z) = 3$, respectively). In the ultrasound model, we set $\sigma_{xy} = \sigma_z = 0.02$, and $\omega_0 = 100$. These parameters were chosen to give a symmetrical travelling wavelet that could approximate a focused ultrasound beam at the focusing region.

The forward problem is simulated for 41 electrode orientations ranging from 0° to 180° in increments of 4.5°. The voltage measured on the homogeneous mesh is subtracted from the signals measured in the presence of an inclusion, leaving only the inclusion's effects in the signal. Two sample measurements at the 45° and 90° are shown in Fig. 2.

Once the voltage measured in the homogeneous mesh is subtracted from the voltage measured in the mesh with inclusion, the peak-to-peak voltage of the resulting signal is calculated and displayed in Fig. 3 (top) as a function of the electrode angle. In doing this only the measured effect of the inclusion remains in the signal. Fig. 3 also shows that when the inclusion conductivity is greater than the background, the signal strength monotonically increases with it. Conversely, when the inclusion conductivity is lower than the background's, the peak-to-peak voltage also increases as the conductivity decreases. To confirm this observation, Fig. 3 (bottom) shows the peak-to-peak voltage difference (mesh with inclusion minus homogeneous mesh voltage) measured at 90°, when the inclusion conductivity is swept from 1/1024 to 1024 times the background conductivity.

The largest magnitude is attained when the measurement electrodes are at 90° and the beam of the ultrasound wave passes directly through all four electrodes. These results confirm that the quadripole electrode configuration can detect the presence of an inclusion and see the greatest signal strength when placed along the propagation axis of the ultrasound wave. Thus the effects of the ultrasound beam and electrode spacing are further investigated.

First the electrodes are held at the fixed position as outlined in Fig. 1 and the frequency is swept from 0.25 MHz to 5 MHz in 200 steps while measuring the peak to peak voltage. In this experiment the width of the ultrasound pulse is not adjusted. Therefore the pulse length remains the same while the number of cycles for one pulse is increased.

The top plot in Fig. 4 shows a global maximum amplitude measured around 0.5 MHz with local maxima at 2 MHz and 3.25 MHz approximately. These peaks correspond to the positions where the electrode spacing is a half multiple of the ultrasound wavelength as this allows the pulse to be at a maximum at one electrode and a minimum at another maximizing the differential measurement. At the lower frequency of 0.5 MHz the wavelength is longer allowing for it to create a larger change in conductivity around the electrode and therefore the strongest induced voltage.

Frequencies lower than 0.25 MHz reach a saturation point as their wavelength are long enough to exceed the z-direction Gaussian envelope of (7) and are attenuated. Therefore it is not possible to lower ultrasound centre frequencies to create maximized signals at low frequencies without further adjusting the parameter of the ultrasound pulse.

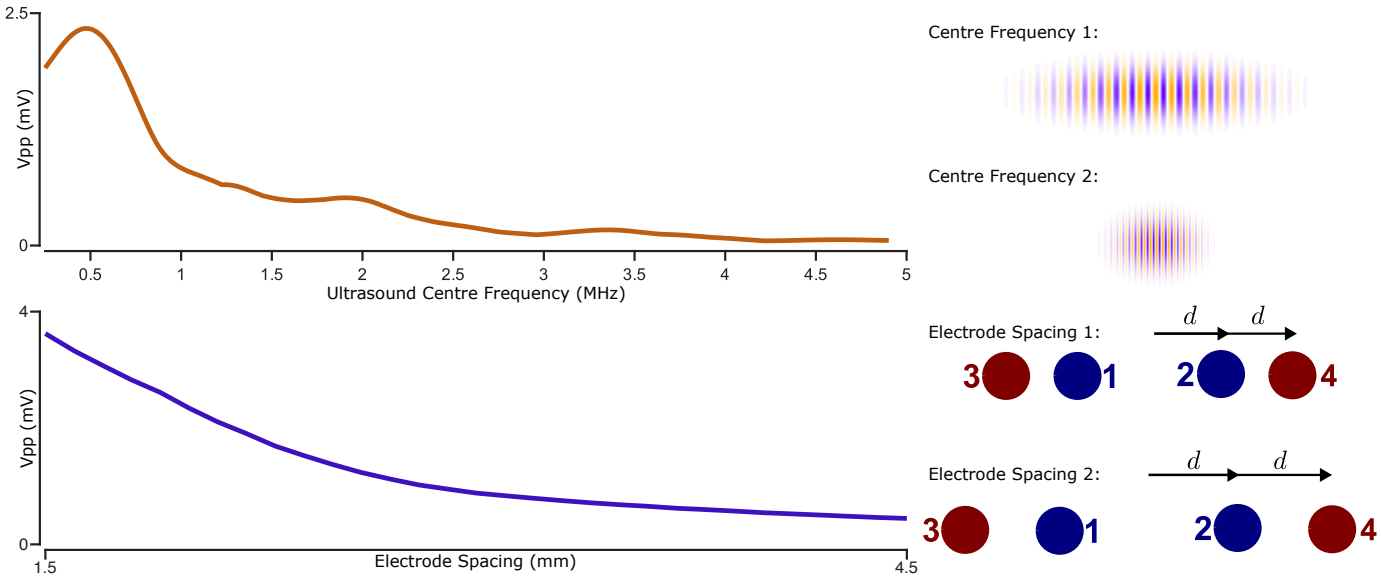

Fig. 4: Peak-to-peak voltage at the measuring electrodes when sweeping the ultrasound centre frequency and the electrode spacing. In the top plot the peak-to-peak voltage is measured while holding the electrode spacing at $d = 2mm$ and adjusting the frequency of the ultrasound pulse from approximately 0.25 MHz until 5 MHz in 200 steps. The bottom plot shows the peak-to-peak voltage measured while holding the frequency at 0.5 MHz and increasing the electrode spacing from $d = 1.5mm$ until $d = 4.5mm$ in steps of $0.1mm$. The top right side of the figure shows the different centre frequencies passing through the electrodes and the bottom right side shows how the electrode configuration changes as the distance d is increased.

Next, at a fixed frequency of 0.5 MHz the electrode spacing is investigated. In this simulation the distance from the centre of the injecting electrodes is set to d and the distance between the measuring electrodes is set to $2d$ as demonstrated in the bottom right of Fig. 4. This maintains the relative spacing of the electrodes from their initial position. Starting from the initial position of $d = 1.5mm$ the electrode spacing is increased until $d = 4.5mm$ in steps of $0.1mm$.

As the electrode spacing is increased, the signal strength measured drops off monotonically as reflected in the lower plot of Fig. 4. This decrease in signal strength is caused by the both the stimulating and measuring electrodes moving farther apart. For the stimulating electrodes this means a decrease in the local electric field strength causing the induced change in voltage from the ultrasound beam to be lower. At a greater distance the measuring electrodes have a lower ability to differentially detect the induced change in voltage created by the simulating electrodes and the ultrasound beam.

IV. Conclusion

In this paper, we propose a finite element model using EIDORS to simulate the AE effect. The effect is captured by simulating a pressure wave propagating through the simulation mesh, represented as a Gabor wavelet whose magnitude alters the local conductivity of mesh elements. While the proposed ultrasound waveform is not based on the acoustic properties of the medium, the formulation allows it to be shaped to match the acoustic pressure distribution of both plane and focused waves. With quadripolar electrodes placed in the mesh, we evaluate the generated AE signal strength for different electrode configurations and compare the results obtained in a homogeneous medium against those in a medium containing an inclusion of altered conductivity. This analysis isolates the effect of the inclusion, as the ability of the system to detect it is the fundamental principle of inverse problems in AET.

The simulation results suggest that the peak AE signal strength is achieved when the stimulating and measuring electrodes are aligned along the z-direction, that is, along the direction of pressure propagation. In this configuration, the measuring electrodes are positioned in the region of highest current density, and therefore, the measured voltages are more susceptible to changes in tissue conductivity. Likewise, the difference in peak-to-peak voltages between the homogeneous case and the inclusion case reaches its maximum for the same electrode configuration.

After determining the configuration that created the maximum signal strength, the centre frequency of the ultrasound was adjusted to investigate how its wavelength affected the measured signal. The the maximum signal was observed at 0.5 MHz, which is when the wavelength is comparable to the size of the electrodes. This suggests that lower frequency ultrasound waves can create larger amplitude signals. However there are additional local peaks seen in the high frequencies ranges. Therefore if an ultrasound wave must be in this region, there are other centre frequencies that maximize signal strength. Additionally when increasing the spacing of the measurement and stimulation electrodes there is a drop off in measurable signal even when the electrodes are inline with

the ultrasound beam. Overall, these findings suggest that for a specific configuration there is an optimal frequency and the spacing of the measurement electrodes should remain as close as possible to maximize the signals strength.

Another finding that was not in the paper's direct focus but warrants further investigation is the richness and variation in the signals with respect to their measurement positions. Visible in Fig. 2, the raw waveforms in columns 1 and 3 exhibit distinct lobes in their signals, corresponding to the modelled ultrasonic waveform passing through the electrodes at these points. When the measuring electrodes are out of the axis of the beam, at 45°, there are only two lobes corresponding to the stimulating electrodes 1 and 2. When they are within the beam, four lobes are seen corresponding to the beam passing through the electrodes 4, 1, 2, and then 3. While these effects are generally removed through the subtraction of the homogeneous signal, they still suggest the possibility of rich extractable features within the raw signals, regardless of signal strength, to support the creation of tomographic images.

These findings can guide the future design of minimal AET systems using only a pair of internal electrodes, potentially embedded in surgical tools such as needles and catheters [8], [4]. Such a system would deliver information directly from within the tissue, addressing the major limitation of reduced sensitivity in deep tissue commonly observed in traditional AET and electrical impedance tomography methods.

REFERENCES

[1] H. Zhang and L. V. Wang, "Acousto-electric tomography," in *Photons Plus Ultrasound: Imaging and Sensing*, vol. 5320. SPIE, 2004, pp. 145–149.

[2] B. Keeshan, A. Adler, and C. Rossa, "Improved configurations for 3d acoustoelectric tomography with a minimal number of electrodes," *IEEE Transactions on Biomedical Engineering*, vol. 70, no. 12, pp. 3501–3512, 2023.

[3] B. Jensen, A. Kirkeby, and K. Knudsen, "Feasibility of acousto-electric tomography," *Inverse Problems*, vol. 40, no. 7, p. 075007, 2024.

[4] R. H. Tan, C. McDermott, and C. Rossa, "A lumped element method for acoustoelectric imaging reconstruction: A numerical study," in *2022 IEEE International Conference on Systems, Man, and Cybernetics (SMC)*. IEEE, 2022, pp. 1798–1803.

[5] P. Kuchment and L. Kunyansky, "2d and 3d reconstructions in acousto-electric tomography," *Inverse Problems*, vol. 27, no. 5, p. 055013, 2011.

[6] C. Li, M. Karamehmedović, E. Sherina, and K. Knudsen, "Levenberg–marquardt algorithm for acousto-electric tomography based on the complete electrode model," *Journal of mathematical imaging and vision*, vol. 63, no. 4, pp. 492–502, 2021.

[7] B. Keeshan, A. Adler, and C. Rossa, "Reduced effective sensitivity of acoustoelectric tomography," *International Journal of Bioelectromagnetism*, vol. 24, 2022.

[8] C. McDermott, H. A. Bidgoli, and C. Rossa, "Observation of the ultrasonic vibration potential with an instrumented coaxial needle probe," in *2023 IEEE International Instrumentation and Measurement Technology Conference (I2MTC)*. IEEE, 2023, pp. 1–6.

[9] Y. Zhou, X. Song, Z. Wang, F. He, and D. Ming, "Multisource acoustoelectric imaging with different current source features," *IEEE Transactions on Instrumentation and Measurement*, vol. 70, pp. 1–9, 2020.

[10] A. Bales-D'Cruze, A. Adler, and C. Rossa, "Lock-in demodulation of pulsed ultrasonic signals in high noise environments," in *2025 IEEE International Conference on Imaging Systems and Techniques (IST)*, 2025, pp. 1–6, ISSN: 2832-4234.

[11] C. Preston, A. M. Alvarez, A. Barragan, J. Becker, W. S. Kasoff, and R. S. Witte, "High resolution transcranial acoustoelectric imaging of current densities from a directional deep brain stimulator," *Journal of neural engineering*, vol. 17, no. 1, p. 016074, 2020.

[12] R. Olafsson, R. S. Witte, S.-W. Huang, and M. O'Donnell, "Ultrasound current source density imaging," *IEEE Transactions on biomedical engineering*, vol. 55, no. 7, pp. 1840–1848, 2008.

[13] J. L. Rintoul, E. Neufeld, C. Butler, R. O. Cleveland, and N. Grossman, "Remote focused encoding and decoding of electric fields through acoustoelectric heterodyning," *Communications Physics*, vol. 6, no. 1, p. 79, 2023.

[14] B. J. Adesokan, K. Knudsen, V. P. Krishnan, and S. Roy, "A fully non-linear optimization approach to acousto-electric tomography," *Inverse problems*, vol. 34, no. 10, p. 104004, 2018.

[15] S. Roy and A. Borzi, "A new optimization approach to sparse reconstruction of log-conductivity in acousto-electric tomography," *SIAM Journal on Imaging Sciences*, vol. 11, no. 2, pp. 1759–1784, 2018.

[16] X. Song, Y. Zhou, R. S. Witte, and D. Ming, "Noninvasive acoustoelectric imaging of resistivity distribution based on lead field theory," *IEEE Transactions on Instrumentation and Measurement*, vol. 68, no. 12, pp. 4779–4786, 2019.

[17] A. Adler and W. R. B. Lionheart, "Uses and abuses of EIDORS: an extensible software base for EIT," *Physiological Measurement*, vol. 27, no. 5, pp. S25–42, 2006.

[18] J. Jossinet, B. Lavandier, and D. Cathignol, "The phenomenology of acousto-electric interaction signals in aqueous solutions of electrolytes," *Ultrasonics*, vol. 36, no. 1, pp. 607–613, Feb. 1998.

[19] J. Jossinet, B. Lavandier, and D. Cathignol, "Impedance modulation by pulsed ultrasound," *Ann. N.Y. Acad. Sci.*, vol. 873, no. 1, pp. 396–407, Apr. 1999.

[20] B. Lavandier, J. Jossinet, and D. Cathignol, "Experimental measurement of the acousto-electric interaction signal in saline solution," *Ultrasonics*, vol. 38, no. 9, pp. 929–936, 2000.